Evaluation of the Interperiod Correlation of Ground-Motion Simulations

by Jeff Bayless and Norman A. Abrahamson

Abstract   We demonstrate that the interperiod correlation of epsilon (ρ_ϵ) is an essential component of ground motions for capturing the variability of structural response that is needed in seismic fragility and seismic risk studies. To perform this demonstration, we generate large suites of scenario ground-motion simulations using the point-source (PS) stochastic method. Two compatible suites of simulations are developed; one suite without any imposed interperiod correlation, and one with Fourier amplitude ϵ sampled from a multivariate normal distribution with covariance specified by our empirical model. We illustrate how the effect of ρ_ϵ propagates through the structural response and into seismic risk calculations. Without the adequate interperiod correlation of ground motions, variability in the structural response may be underestimated. This leads to structural fragilities that are too steep (underestimated dispersion parameter β) and propagates to nonconservative estimates of seismic risk.

To assess the current state of multiple existing ground-motion simulation methods, we evaluate their interfrequency correlations and compare with empirical models. None of the six finite-fault simulation methods tested adequately capture the interperiod correlations over the entire frequency range evaluated, although several of the methods show promise, especially at low frequencies. Using the correlation of the Fourier spectra provides the developers of the simulation methods better feedback in terms of how they can modify their methods, which is unclear when using response spectra comparisons. Based on the relative differences in the correlations of the Song (2016) source method, it appears that changes to the rupture generator may be the most promising approach to modifying the long-period interperiod correlations.

Introduction

Residuals from empirical ground-motion models (GMMs, also known as ground-motion prediction equations [GMPEs]) are typically partitioned into between-event residuals (δB) and within-event residuals (δW), following the notation of Al Atik *et al.* (2010). For large numbers of recordings per earthquake, the between-event residual is approximately the average difference in logarithmic space between the observed intensity measure (IM) from a specific earthquake and the IM predicted by the GMM. The within-event residual (δW) is the difference between the IM at a specific site for a given earthquake and the median IM predicted by the GMM plus δB. By accounting for repeatable site effects, δW can further be partitioned into a site-to-site residual ($\delta S2S$) and the single-station within-event residual (δWS) (e.g., Villani and Abrahamson, 2015).

The residual components δB, $\delta S2S$, and δWS are well represented as zero mean, independent, normally distributed random variables with standard deviations τ, ϕ_{S2S}, and ϕ_{ss}, respectively (Al Atik *et al.*, 2010). These GMM residual components are converted to epsilon (ϵ_B, ϵ_{S2S}, and ϵ_{WS}) by normalizing the residuals by their respective standard deviations.

Because of the normalization, the random variables ϵ_B, ϵ_{S2S}, and ϵ_{WS} are represented by standard normal distributions (mean = 0, variance = 1). If the total residual is used, then the resulting ϵ_{total} will, in general, not have zero mean due to the uneven sampling of recordings per earthquake in the data set.

For a given recording, the values of ϵ at neighboring periods (T) are generally correlated. For example, if a ground motion is stronger than average at $T = 1.0$ s, then it is likely to also be stronger than expected at nearby periods, for example, $T = 0.8$ s or $T = 1.2$ s; however, for a widely spaced period pair (e.g., $T = 10.0$ s compared with $T = 1.0$ s), the ϵ values will be weakly correlated. The interperiod correlation coefficient ρ quantifies the relationship of ϵ values between periods for a given recording.

The correlation coefficient of two random variables is a measure of their linear dependence. In this case, ϵ calculated from a large set of ground motions at different frequencies (f) are random variates. The correlation coefficient between $\epsilon(f_1)$ and $\epsilon(f_2)$ can be estimated using a maximum-likelihood estimator, the Pearson-product-moment correlation coefficient
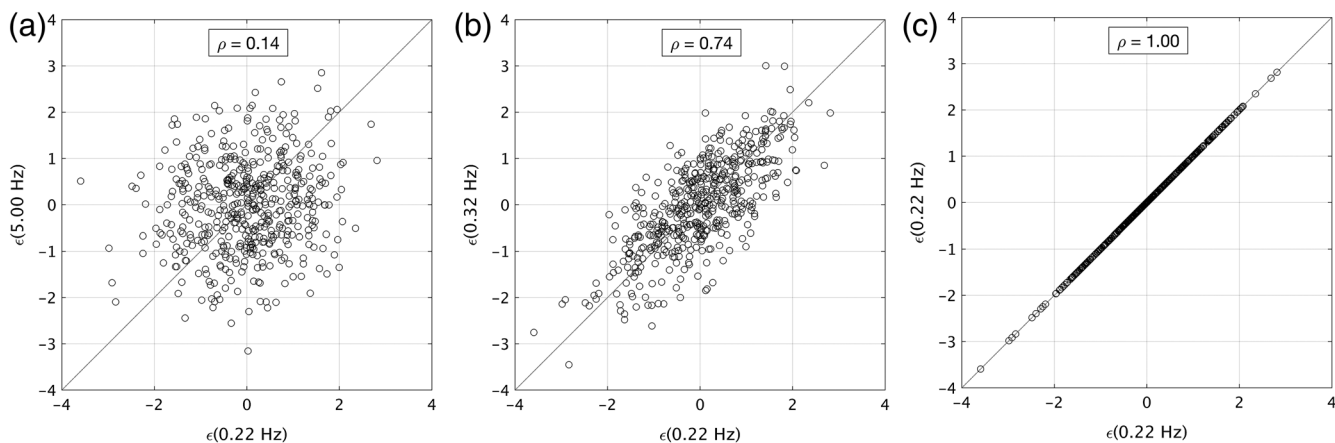
Figure 1. ϵ values at pairs of frequencies calculated from a database of ground motions, exhibiting the correlation dependent on frequency spacing. (a) $f_1 = 0.2$ Hz and $f_2 = 5.0$ Hz. (b) $f_1 = 0.2$ Hz and $f_2 = 0.3$ Hz. (c) $f_1 = 0.2$ Hz and $f_2 = 0.2$ Hz.

ρ (Fisher, 1958). The correlation coefficient for a sample of ϵ at frequencies f_1 and f_2 is given as follows:

$$\rho_{\epsilon(f_1),\epsilon(f_2)} = \frac{\text{cov}(\epsilon(f_1),\epsilon(f_2))}{\sigma_{\epsilon(f_1)}\sigma_{\epsilon(f_2)}}$$
$$= \frac{\sum_{i=1}^{n}(\epsilon_i(f_1) - \overline{\epsilon(f_1)})(\epsilon_i(f_2) - \overline{\epsilon(f_2)})}{\sqrt{\sum_{i=1}^{n}(\epsilon_i(f_1) - \overline{\epsilon(f_1)})^2}\sqrt{\sum_{i=1}^{n}(\epsilon_i(f_2) - \overline{\epsilon(f_2)})^2}}, \quad (1)$$

in which cov is the covariance, σ is the standard deviation, n is the total number of observations, i is the ith observation of ϵ, and $\overline{\epsilon(f_1)}$ and $\overline{\epsilon(f_2)}$ are the sample means of ϵ at frequencies f_1 and f_2, respectively. In our applications, $\bar{\epsilon}$ is equal to zero, indicating that the GMM is unbiased. The relation for $\rho_{\epsilon(f_1),\epsilon(f_2)}$ given in equation (1) is reciprocal; the correlation coefficient between two given frequencies is the same regardless of which frequency is the conditioning frequency. To account for all residual terms, the total correlation is calculated as

Jayaram, 2008; Goda and Atkinson, 2009; Abrahamson *et al.*, 2014; Cimellaro, 2013; Baker and Bradley, 2017). Recently, correlation models for ϵ from Fourier amplitude spectra (FAS) have also been developed (e.g., Stafford, 2017; J. Bayless and N. A. Abrahamson, unpublished manuscript, 2018, see Data and Resources).

Physical Meaning and Relevance of ρ_ϵ

Because larger than average ground motions tend to be from local spectral peaks and lower than average ground motions tend to be from local spectral troughs, the parameter ϵ is an indicator of the peaks and troughs at a given frequency in a spectrum. Because ρ_ϵ is a measure of the linear dependence of ϵ between two frequencies, ρ_ϵ characterizes the relative width of these extrema. For example, very high ρ_ϵ (values close to one) over broad frequency pairs indicate wide peaks and troughs in the spectra, leading to smoother undulating spectra. Conversely, very low ρ_ϵ (values close to zero)

$$\rho_{\epsilon,\text{total}}(f_1, f_2) = \frac{\rho_B(f_1, f_2)\tau(f_1)\tau(f_2) + \rho_{S2S}(f_1, f_2)\phi_{S2S}(f_1)\phi_{S2S}(f_2) + \rho_{WS}(f_1, f_2)\phi_{ss}(f_1)\phi_{ss}(f_2)}{\sigma(f_1)\sigma(f_2)}, \quad (2)$$

in which $\rho_B(f_1, f_2)$ is the correlation of the normalized between-event residuals, $\rho_{S2S}(f_1, f_2)$ is the correlation of the normalized site-to-site residuals, and $\rho_{WS}(f_1, f_2)$ is the correlation of the normalized single-station within-event residuals.

Using a database of residuals, the calculation of $\rho_{\epsilon(f_1),\epsilon(f_2)}$ can be repeated for every frequency pair of interest. Figure 1 shows a graphical representation of this step at three example frequency pairs. The resulting correlation coefficients for each pair of frequencies can be saved as tables (e.g., Al Atik, 2011; Jayaram *et al.*, 2011; Abrahamson *et al.*, 2014; Akkar *et al.*, 2014; Azarbakht *et al.*, 2014), or can be empirically modeled. For modern GMMs, models of the correlation of ϵ are commonly created for pseudospectral acceleration (PSA) (e.g., Baker and Cornell, 2006; Baker and

between neighboring frequency pairs indicate very narrow peaks and troughs, leading to noisy looking spectra.

The generic term spectra can refer to either PSA or FAS. PSA spectra are the peak response from a single-degree-of-freedom oscillator system. PSA spectra are influenced by a range of frequencies, and the breadth of that range is dependent on the oscillator period (J. Bayless and N. A. Abrahamson, unpublished manuscript, 2018, see Data and Resources) and on the damping. The FAS provides a more direct representation of the frequency content of the ground motions, and because the Fourier transform is a linear operation, the FAS is a much more straightforward representation of the ground motion and is better understood by seismologists. This simpler behavior makes the FAS preferable over PSA for incorporat-

ing interperiod correlation into numerical methods for ground-motion simulations, and it is the IM we adopt in this article.

Because ρ_ϵ is a measure of the width of spectral peaks, it has relevance in dynamic structural response. For linear response, a structure will be sensitive to the frequency content over a range of frequencies about the natural frequency of the structures. For the uncorrelated case, if the ϵ value at the natural frequencies is a high-positive value (corresponding to a peak), the values of ϵ at the nearby frequencies will be randomly high or low so the response of the structure will increase by a small factor; however, for the correlated case, the values of ϵ at the nearby frequencies will tend to also be positive values so the response of the structure will increase by a larger factor relative to the uncorrelated case. During nonlinear seismic response, the effect of the correlation can be even greater than for linear response. For nonlinear response, structures can experience softening characterized by elongation of their natural vibration period (Bradford, 2007; Lin *et al.,* 2008). This occurs when damage to the structural elements leads to large strains, which reduce the effective stiffness and increases effective damping. As a structure softens, its effective fundamental period increases and the response will depend on if the structure is softening into a peak or a trough in the spectrum. For the correlated case, the chance of softening into a peak or a trough will depend on the breadth of a ground-motion spectral peak or trough, thereby affecting the structural response. The aggregate effect is that the variability in structural response is higher for ground motions with realistic ρ_ϵ than for ground motions with unrealistically low ρ_ϵ, as we demonstrate in the following sections of this article.

Article Organization

In this article, we demonstrate that the characteristics of the correlation of the FAS ρ_ϵ have a significant effect on structural fragilities, and evaluate if the interfrequency correlation is properly captured in existing ground-motion simulation methods. We begin with a short summary of the four main components of Pacific Earthquake Engineering Research Center's (PEER) performance based earthquake engineering (PBEE) framework, and we use this framework to define structural risk in terms of structural fragility and seismic hazard. We then describe a method for developing structural fragilities from ground-motion simulations and show that ρ_ϵ is a critical feature of ground motions that should be considered as a validation parameter for numerical simulations. A method is developed for generating simulated ground motions with appropriate ρ_ϵ. We present an example of seismic risk for a generic site in southern California using this ground-motion simulation method, and compare with results using the same simulation method but without the correlation. We illustrate how the effect of ρ_ϵ propagates through to the structural response variability and then into seismic risk. Finally, we evaluate the interfrequency correlations of multiple existing ground-motion simulation methods, and compare the results with empirical models for the correlation.

Structural Risk in PBEE

Following Moehle and Deierlein (2004), PEER's probabilistic framework for PBEE is separated into four main analysis steps: hazard analysis (characterized by a ground-motion IM), structural analysis (characterized by an engineering demand parameter [EDP]), damage analysis (characterized by damage measure), and loss analysis (characterized by a decision variable). Using this framework, one can focus solely on the first two analysis steps to estimate the EDP hazard, defined as the mean annual rate of exceeding a given structural response level. The EDP hazard is given as,

$$\lambda(\text{EDP} > z) = \int_x P(\text{EDP} > z | \text{IM} = x) \left| \frac{d\lambda(\text{IM} > x)}{dx} \right| dx, \quad (3)$$

in which $\lambda(\text{EDP} > z)$ is the mean annual rate of exceeding EDP value z. $P(\text{EDP} > z | \text{IM} = x)$ is the structural fragility, which is the probability of exceeding EDP value of z given $\text{IM} = x$. $\lambda(\text{IM} > x)$ is the mean annual rate of exceeding IM value x, and $d\lambda$ is the rate of occurrence of IM value x, which is the slope of the IM hazard curve. Therefore, the EDP hazard for exceeding a specified value z is comprised of two quantities: the structural fragility, and the ground-motion hazard, integrated over all relevant IM levels x.

In this article, the selected IMs are 5% damped PSA and FAS, and the selected EDP is the maximum interstory drift ratio (MIDR), but it is noted that the EDP risk framework (equation 2) is applicable to other appropriate IMs and EDPs. As interstory drift is commonly adopted as the EDP; it is common to refer to the EDP hazard as drift hazard.

Structural Risk Using Ground-Motion Simulations

Fragilities Developed from Simulations

A fragility function specifies the probability of a structural consequence (EDP) as a function of the ground-motion intensity. Fragility functions can be obtained using the incremental dynamic analysis (IDA) procedure as a means of integrating structural simulations and ground motions (Moehle and Deierlein, 2004; Baker, 2013). With this procedure, using a suite of ground motions, structural response calculations are carried out in which the building is subjected to the input ground motions having a specified IM amplitude, and the fraction of the ground motions exceeding the specified EDP are counted. The process is repeated at increasing IM levels to obtain the probability of exceeding the EDP at discrete IM amplitudes. A lognormal cumulative distribution function (CDF) can be fit to the probabilities, for example,

$$P_{\text{fit}}(\text{EDP} > z | \text{IM} = x) = \Phi \left[\frac{\ln(x) - \ln(\alpha)}{\beta} \right], \quad (4)$$

in which $P_{\text{fit}}(\text{EDP} > z | \text{IM} = x)$ is the fitted fragility function, Φ is the CDF of the standard normal distribution, α is the IM with median fragility, β is the logarithmic standard
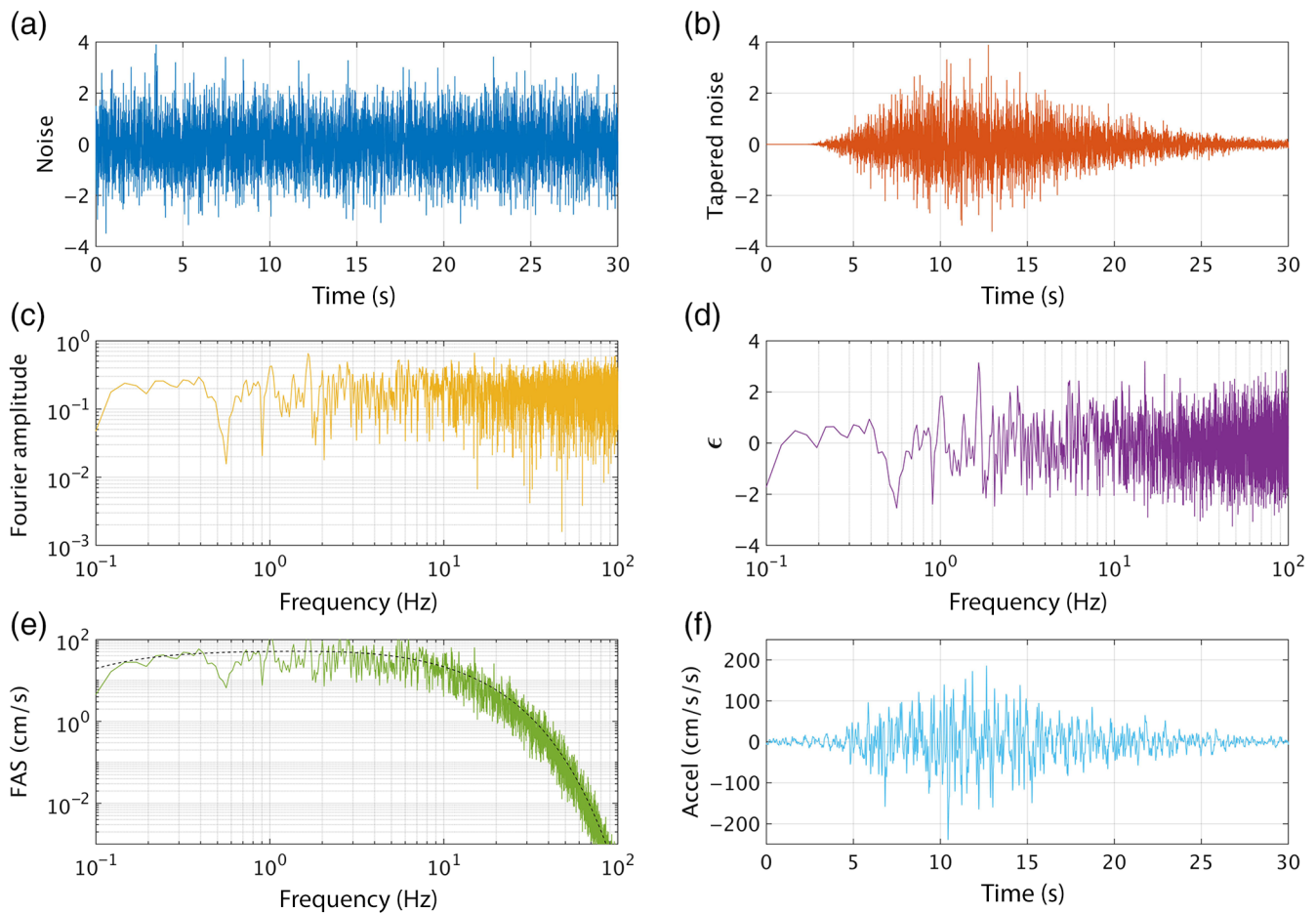
Figure 2. Illustration of the Boore (2003) procedure for simulating acceleration time series using the point-source (PS) stochastic method. (a) Generate normally distributed time-domain noise, and (b) apply a time-domain taper with duration consistent with the scenario considered. (c) Fourier transform the tapered noise into the frequency domain, and (d) normalized the Fourier amplitude spectra (FAS) of the noise by the square root of the mean power, such that the FAS has mean power of one (the natural logarithm of these values is shown). (e) Shape the normalized FAS to the PS FAS of the considered scenario, and (f) inverse Fourier transform to the time-domain using the phase angles from the tapered time domain noise. The color version of this figure is available only in the electronic edition.

deviation of the CDF, and α and β are estimated from the IDA results. This method is demonstrated in this article. An alternative to IDA is the multiple stripe analysis (MSA) method, in which ground motions selected specifically for the IM amplitude are analyzed, rather than scaling one set of ground motions for multiple IM amplitudes (Baker, 2013). MSA uses scenario-specific ground motions for each IM level, but because the hazard at long return periods is usually driven by increasing epsilon, not magnitude, the IDA approach has merit. The fundamental impact of the correlation can be demonstrated using an IDA, so this is the approach we take in the following example.

Incorporating ρ_ϵ into Ground-Motion Simulations

The point-source (PS) stochastic method for simulating earthquake ground motions, which is based on the pioneering work of Brune (1970), Hanks and McGuire (1981), and Boore (1983), among others, has been developed and refined

over several decades. David Boore formalized the method and extended it to the simulation of acceleration time series (Boore, 1983, 2003). With the Boore (2003; hereafter, Boore03) method, a simulated time series is produced using a seismological model of the Fourier amplitude spectrum and assuming the spectrum is distributed with random phase angles over a time duration related to the earthquake magnitude and the distance between the source and site. Boore (2003) gives a comprehensive description of the method; we provide only a brief summary here.

The classic procedure starts by generating normally distributed noise (Fig. 2a) and applying a time-domain taper with duration consistent with the scenario being considered (Fig. 2b). The tapered noise is transformed into the frequency domain (Fig. 2c), and the FAS of the noise is normalized by the square root of the mean power, such that the FAS has mean power of one (Fig. 2d showing the natural logarithm of these values). The normalized FAS is then shaped to the PS Fourier
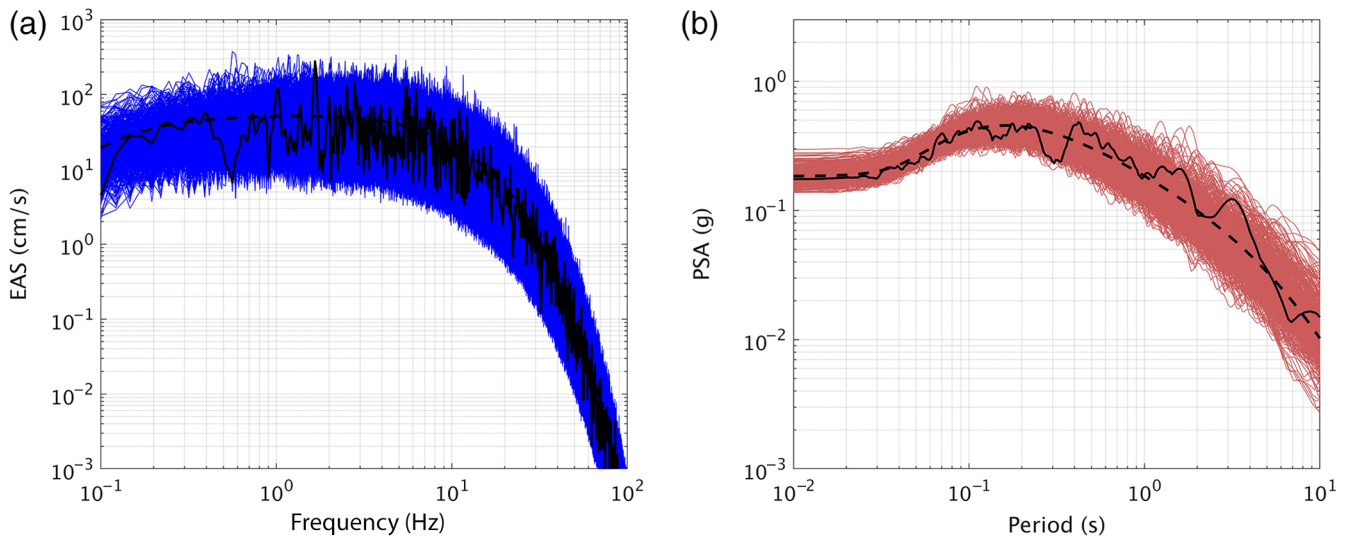
Figure 3. A suite of 500 uncorrelated ground-motion simulations for an **M** 7.0 scenario at 30 km. (a) FAS realizations (thin lines), and the PS scenario spectrum in dashed line type. (b) Pseudospectral acceleration (PSA) spectra realizations (thin lines) and the random vibration theory (RVT) spectrum in dashed line type. One realization is identified with bold line type. The color version of this figure is available only in the electronic edition.

amplitude spectrum of the considered scenario (Fig. 2e), and inverse transformed to the time domain using the phase angles from the tapered time-domain noise (Fig. 2f).

The Boore03 procedure generates ϵ values from time-domain white noise, resulting in ϵ with no correlation between frequencies. To generate simulated time series with realistic interperiod correlation, we modify the Boore03 procedure in the following ways. First, we make use of the symmetric, positive definite covariance matrix ($\mathbf{\Sigma}$) for the interfrequency $\rho_{\epsilon,\text{total}}$ of FAS that the authors have developed in J. Bayless and N. A. Abrahamson (unpublished manuscript, 2018, see Data and Resources). This matrix is factorized using the Cholesky decomposition $\mathbf{\Sigma} = \mathbf{LL}^T$, in which $\mathbf{L}$ is a lower triangular matrix (Seydel, 2012). Then, the zero-mean correlated random variables $\mathbf{Y}$ can be calculated as $\mathbf{Y} = \mathbf{LZ}$, in which $\mathbf{Z}$ are independent random variables drawn from a standard normal distribution. The random variables $\mathbf{Y}$ are then normally distributed with zero mean and covariance matrix $\mathbf{\Sigma}$. In Figure 2d, ϵ values are replaced with random numbers sampled in this fashion. We then multiply the sample ϵ by a standard deviation equal to 0.65 (ln units). The value of 0.65 is consistent with the standard deviation of the FAS that results from the Boore03 procedure (Fig. 2d), which is not sensitive to the time-domain variance of input white noise (Fig. 2b). Finally, we continue with the Boore03 recipe to generate time series with realistic interfrequency ρ_{ϵ} of FAS. This procedure for creating simulated time series with realistic interperiod correlation is similar to the method described in Stafford (2017).

Using these modifications, we have two simulation procedures: the original Boore03 method and the Boore03 method modified to include the interperiod correlation of epsilon. An individual realization of each procedure results in a pair of compatible acceleration time series. Both have similar phasing, duration, frequency content, and amplitudes.

Individual realizations of correlated ϵ may be positive or negative for frequency bands, but as the sample size is increased, the sampled ϵ have the intended standard normal parameter values.

Example Application

In the following example, we develop structural fragilities using an IDA with two sets of ground motions created using the two simulation procedures described in the Incorporating ρ_{ϵ} into Ground-Motion Simulations section. The first set of ground motions has near-zero interperiod correlation and the second set has realistic interperiod correlation. We develop suites of 500 uncorrelated and correlated ground motions using the same PS Fourier amplitude spectrum as the basis for the ground-motion amplitudes.

Both suites of simulations have similar ground-motion distributions in FAS space (approximately 0.65 ln units), as shown in Figures 3 and 4, respectively. To obtain PSA, we perform the inverse Fourier transform to get acceleration time histories, and calculate the response spectrum. In Figures 3b and 4b, we also plot the random vibration theory (RVT) spectrum derived from seismological parameters consistent with the PS spectrum (Boore and Thompson, 2012). The median PSA of the suite of 500 ground motions closely matches the RVT spectrum in both cases.

Although they have the same median, Figures 3 and 4 illustrate the substantial differences in the distribution of PSA between the uncorrelated and correlated ground-motion sets. This happens because PSA spectra are influenced by a range of frequencies. As described previously, considering broad (highly correlated) spectra, the ground motions with extreme FAS ϵ at a given period generally stay extreme over the range of periods influenced by the response spectrum cal-
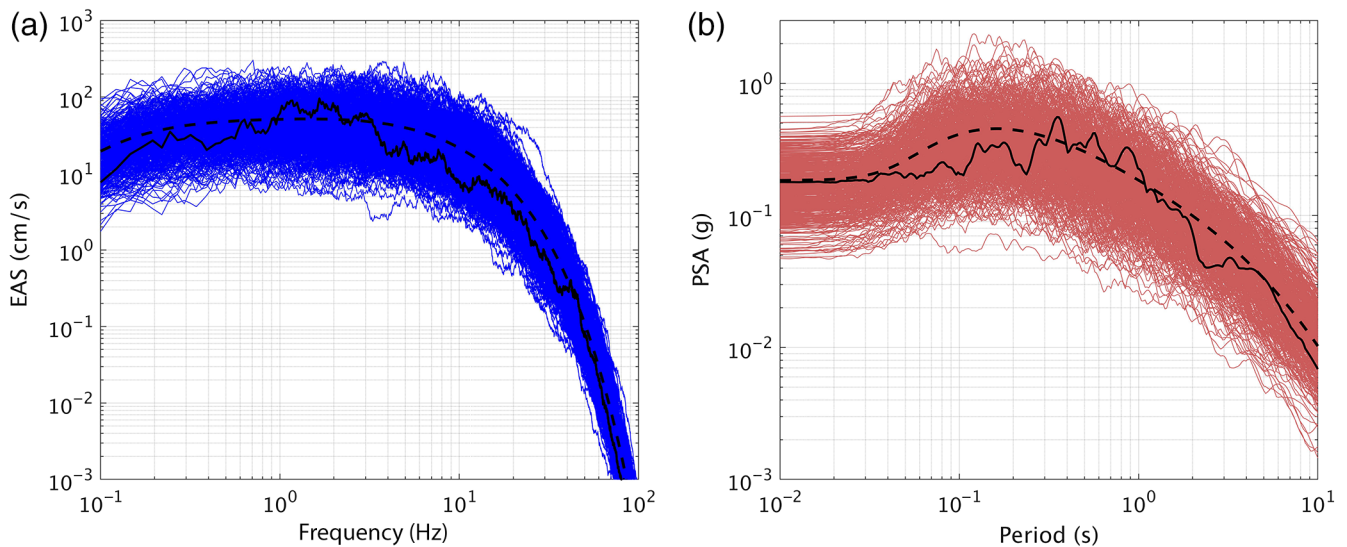
Figure 4. Similar to Figure 3, but using the correlated ground-motion simulations procedure. The color version of this figure is available only in the electronic edition.
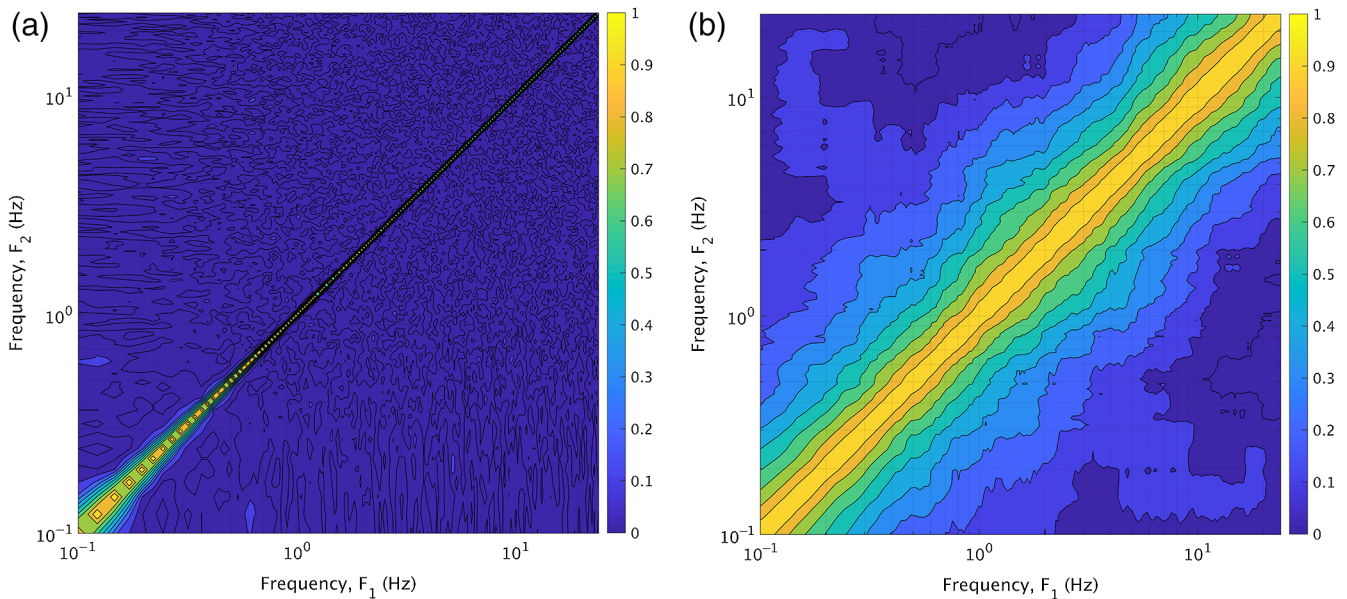
Figure 5. ρ_ϵ of FAS contours over 0.1–24 Hz from (a) the suite of 500 uncorrelated ground-motion simulations and (b) the suite of 500 correlated ground-motion simulations. The color version of this figure is available only in the electronic edition.

culation (i.e., troughs remain in troughs and peaks remain in peaks). The aggregate effect is that the variability in PSA is higher for ground motions with realistic ρ_ϵ than for ground motions with low ρ_ϵ. The response spectrum is a simplified version of a real structure, and therefore its behavior mimics what we expect to see with the complete structural analysis.

As a verification check, we backcalculate the ρ_ϵ of FAS from the suite of 500 simulated time histories, using the PS spectrum as the reference model for calculating residuals. These ρ_ϵ are summarized for the two suites of ground motions in Figure 5. These figures are symmetric about the 1:1 line because the correlation coefficient between two frequencies

is the same regardless of which frequency is the conditioning frequency. As shown in Figure 5a, the Boore03 procedure (uncorrelated) simulations exhibit near-zero correlation between frequencies. The correlated set of ground motions (Fig. 5b) have ρ_ϵ of FAS consistent with the J. Bayless and N. A. Abrahamson (unpublished manuscript, 2018, see Data and Resources) model imposed on the Fourier amplitudes, as expected.

Example Application: Structural Models

We use the open-source finite-element platform, Open-Sees (McKenna *et al.*, 2010), to model the structures and to perform the dynamic nonlinear structural analyses. The fra-
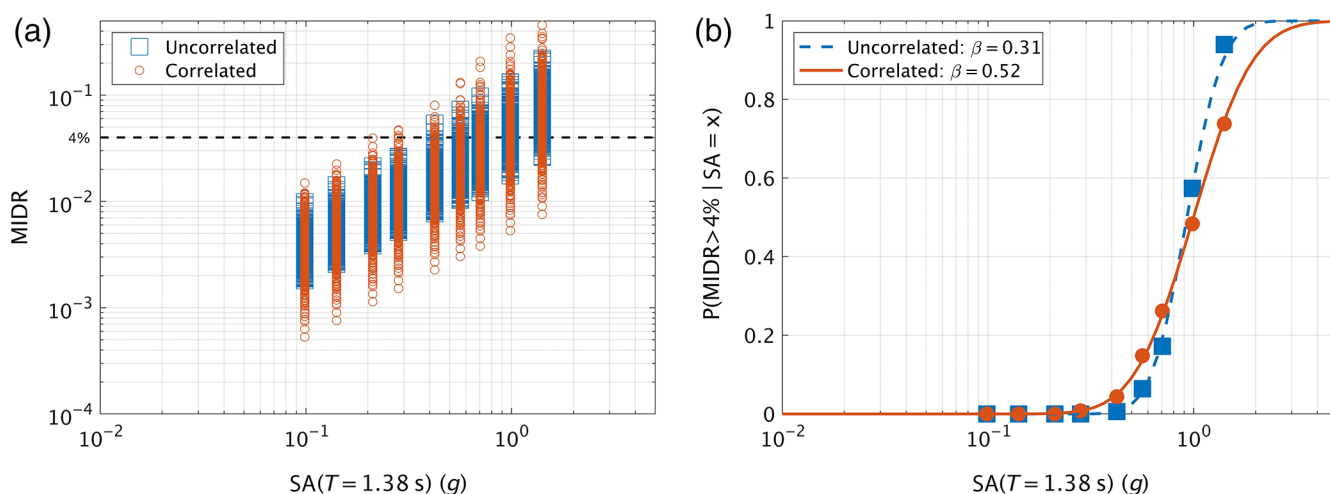
Figure 6. (a) Maximum interstory drift ratio (MIDR) results of the structural analysis for suites of 500 ground motions at. (b) MIDR > 4% probabilities (symbols) and the fitted Cumulative distribution function (CDF) fragility functions (lines). The color version of this figure is available only in the electronic edition.

gility results presented in this article are for the six-story steel special moment resisting frame (SMRF) building model described in Kalkan and Kunnath (2006). Because the impact of the correlation is related to structural softening, we analyzed structures with varying fundamental periods to confirm that our observations are not specific to just one type of structure or fundamental period. In addition to the six-story steel building, we also tested a 12-story reinforced concrete building (Heo, 2009) and a typical California Department of Transportation highway overcrossing (Kunnath *et al.*, 2008). These alternate structures gave similar results to the Kalkan and Kunnath (2006) model.

The Kalkan and Kunnath (2006) building model is based on an existing building located in Burbank, California. The existing building was designed as described by Kalkan and Kunnath (2006), "in accordance with UBC (ICBO, 1973) requirements. The rectangular plan of the building measures 36.6 m by 36.6 m with an 8.2 cm thick lightweight concrete slab over 7.5 cm metal decking. The primary lateral load-resisting system is a moment frame around the perimeter of the building. Interior frames are designed to carry only gravity loads. All columns are supported by base plates anchored on foundation beams, which in turn are supported on a pair of 9.75 m, 0.75 m diameter concrete piles." (p. 371). The building was instrumented by the California Strong Motion Instrumentation Program and recorded the response of the 1987 Whittier Narrows, 1991 Sierra Madre, and 1994 Northridge earthquakes.

The OpenSees computer models of this structure were previously developed by Kunnath *et al.* (2004) and Kalkan and Kunnath (2006), including calibration of the models to match the observed response with the simulated response. The 2D frame model used here is summarized by Kalkan and Kunnath (2006): "A force-based nonlinear beam-column element that utilizes a layered "fiber" section is utilized to model all components of the frame model. A fiber section

model at each integration point, which in turn is associated with uniaxial material models and enforces Bernoulli beam assumptions for axial force and bending, represents the force-based element. Centerline dimensions were used in the element modeling. One half of the total building mass was applied to the frame distributed proportionally to the floor nodes. Modeling of the members and connections was based on the assumption of stable hysteresis derived from a bilinear stress-strain model. The columns were assumed to be fixed at the base level." (p. 372). For additional model properties, the reader is referred to Kalkan and Kunnath (2006).

Example Application: Results

Following the IDA approach, these sets of ground motions are scaled and numerical structural simulations are carried out using OpenSees. The fragility results presented herein are for the six-story steel SMRF building model described in Kalkan and Kunnath (2006). The IDA results are presented in Figure 6, in which squares represent data from the uncorrelated simulations and circles represent the correlated simulations. For each PSA level (at the fundamental structural period; $T = 1.38$ s), the fraction of the ground motions exceeding 4% MIDR is counted. The process is repeated over multiple IM levels to obtain the probability of exceeding 4% MIDR at the discrete IM amplitudes. We optimize the lognormal CDF parameters α and β to fit these probabilities in log space. The least-squares fit is performed in logarithmic space to focus the fit on the low end tail of the CDF, which controls the risk.

As expected, the median structural response is similar between the correlated and uncorrelated ground-motions sets, but the standard deviations of the structural responses are significantly different. For the presented results, the log-normal CDF dispersion parameter β is 0.31 for the uncorrelated ground motions and 0.52 for the correlated ground motions (comparable to the building code value 0.6; Ameri-
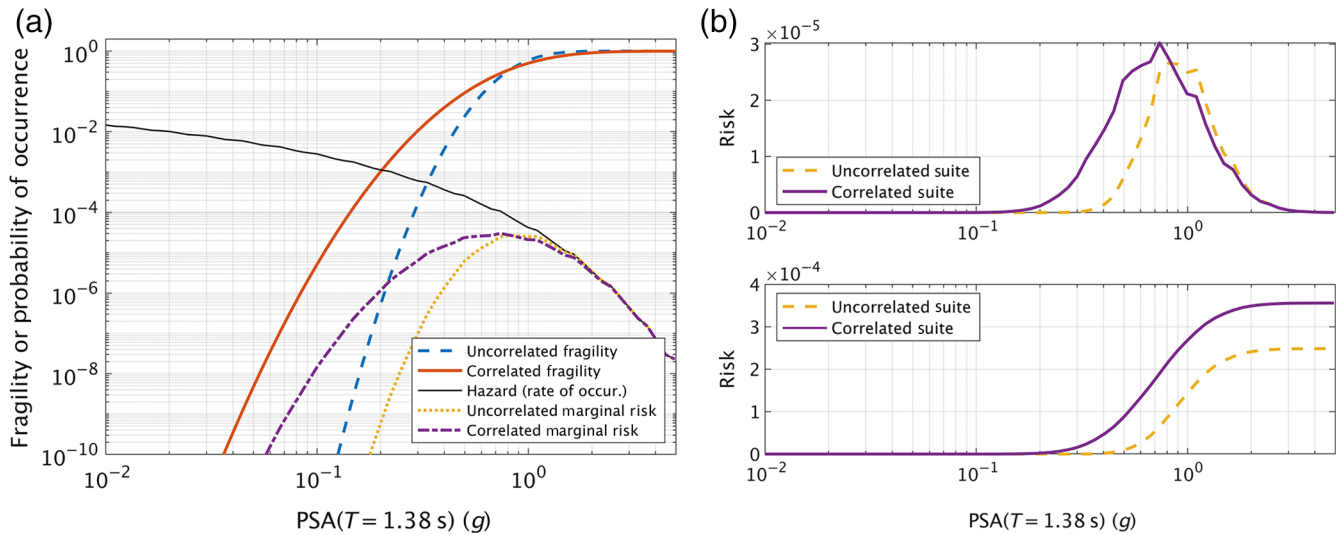
Figure 7. (a) Combining the seismic hazard occurrence and MIDR > 4% fragilities to get the engineering demand parameter (EDP) hazard. (b) The marginal risk (top) and cumulative marginal risk (bottom) on linear scales. The color version of this figure is available only in the electronic edition.

can Society of Civil Engineers [ASCE], 2016). Larger β values mean flatter fragility curves with higher probabilities of failure at the lower IM levels.

We combine the structural fragilities with the seismic hazard to calculate the EDP hazard using equation (3). The results are shown in Figure 7, in which Figure 7a compares the structural fragilities and marginal risk on a logarithmic vertical axis. Plotting them this way illustrates the consequential differences between them at moderate IM levels, in which the hazard is higher, and the risk is sensitive to the fragility. To calculate the risk from the EDP hazard, we assumed a step function of the DMs (usually collapse) as a function of EDP fragility. Figure 7b compares the marginal and cumulative marginal risk on a linear scale for the two ground-motion sets. For this case, the highest marginal risk comes from PSA ($T = 1.38$ s) levels less than 1g. We computed structural risk for four damage states using MIDR exceedances of 0.5%, 1%, 2%, and 4% (Table 1). For the MIDR > 4% case, the structural risk calculated using the ground motions with realistic interperiod correlations is a factor of 1.43 higher than the risk calculated using uncorrelated ground motions, which corresponds to approximately the difference between 4000- and 2800-yr return period for MIDR > 4%.

Evaluating the Correlation of Existing Ground-Motion Simulations

In the Example Application: Results section, we showed that the interfrequency correlation of simulated ground motions is important for capturing the variability of structural response, and therefore impacts the risk. In this section, we evaluate the interfrequency correlations of multiple existing ground-motion simulation methods and compare with empirical models. We outline the procedure used to calculate the correlations and apply it to suites of ground-motion simulations calculated using several established simulation methods. The simulations used are from the Southern California Earthquake Center (SCEC) Broadband Platform (BBP, Maechling *et al.*, 2015) and from the Lawrence Livermore National Laboratory (LLNL).

Simulation Methods Evaluated

The SCEC BBP is a collaborative software development project, with the objective to integrate complex scientific codes for generating broadband ground motions for earthquakes. Contributions come from many scientific groups including researchers, practitioners, and software developers. On the BBP, the modular components include rupture generation, low- and high-frequency seismogram synthesis, nonlinear site effects, and visualization (Maechling *et al.*, 2015). Collections of these modules by different groups form alternate simulation methods. All of the BBP simulations we evaluate are based on regionalized 1D (plane layered) earth models with engineering bedrock surface conditions, and do not model near-surface site effects. The currently implemented methods include EXSIM (Atkinson and Assatourians, 2015), GP (Graves and Pitarka, 2015), SDSU (Olsen and Takedatsu, 2015), and UCSB (Crempien and Archuleta, 2015).

Table 1
Structural Risk for Damage States with Maximum Interstory Drift Ratio (MIDR) Exceedances of 0.5%, 1%, 2%, and 4%

Ground-Motion Suite	MIDR ≥ 0.5%	MIDR ≥ 1%	MIDR ≥ 2%	MIDR ≥ 4%
Correlated	1.44×10^{-2}	5.12×10^{-3}	1.42×10^{-3}	3.56×10^{-4}
Uncorrelated	1.25×10^{-2}	4.26×10^{-3}	1.11×10^{-3}	2.49×10^{-4}
Ratio	1.15	1.20	1.28	1.43

The process described in Dreger *et al.* (2015) established that specific methods (overdefined period and magnitude ranges) on the BBP produce median results suitable for use in engineering applications. This validation exercise, driven by the needs of two major ground-motion hazard projects, evaluated the performance of the different simulation methods in matching median PSA (RotD50 component), using both recorded earthquakes and GMMs for validation. For validating the simulations against data, nine events in active crustal regions were considered: 2008 Chino Hills, 2007 Alumn Rock, 1987 Whittier Narrows, 1986 North Palm Springs, 1994 Northridge, 1989 Loma Prieta, 1992 Landers, 2000 Tottori, and 2004 Niigata (Goulet *et al.*, 2015). These nine events are the simulations utilized herein, calculated with SCEC BBP v. 16.5. We also evaluate the SONG (Song, 2016) method, which is implemented on the SCEC BBP, but has not undergone the Dreger *et al.* (2015) validation exercise.

We also evaluated a set of simulations calculated by LLNL, which are described in Rodgers *et al.* (2018). LLNL simulated ground motions for an **M** 7.0 scenario earthquake on the Hayward fault using 3D earth structure and surface topography, with the open-source finite-difference wave propagation code SW4. These simulations span frequencies from 0 to 4 Hz and the computational domain covers a 120 by 80 km area surrounding the fault, with a dense grid of simulation sites (2301 in total) at the ground surface throughout the domain. The deterministic source description was created using the GP rupture generator. For more details on the simulation method and assumptions, the reader is referred to Rodgers *et al.* (2018).

Previous Work

Others have studied the correlation of PSA of simulated ground motions (Burks and Baker, 2014), and the structural response of buildings to simulated and recorded ground motions, considering differences in epsilon (Tothong and Cornell, 2006). Tothong and Cornell concluded that the PSA for positive epsilon records (simulated using the PS stochastic method) drops off rapidly as the period ratio increases or decreases as compared with the as-recorded motions, resulting in an underestimation of the inelastic response of structures. This conclusion is consistent with our findings. More recently, Burks and Baker (2014) evaluated the interfrequency correlations of response spectra using a subset of the Dreger *et al.* (2015) SCEC simulations, calculated using BBP v. 11.2. Burks and Baker (2014) used simulations of the 1989 Loma Prieta earthquake (40 stations on rock site conditions), and obtained simulations performed by three groups: EXSIM, CSM (Anderson, 2015), and GP. We summarize the conclusions from Burks and Baker (2014) as follows: the GP correlations were generally too low at short periods (the less theoretically rigorous, or stochastic portion) but had some correlation at long periods (the deterministic portion). The EXSIM method correlations were too low at all periods, and the CSM correlations were high at all periods

relative to the empirical models and data. The Goulet *et al.* (2015) SCEC validation exercise did not evaluate the CSM method (Dreger and Jordan, 2014), so we did not include it in our analysis. In future work, we would like to evaluate the correlation of this method because the conclusions from Burks and Baker (2014) indicate this method could provide some insight on the features controlling the correlation. Following a description of our procedure, we compare the Burks and Baker (2014) conclusions with our results.

Procedure

To calculate ρ_ϵ of the simulations, we begin by calculating the FAS from the simulated acceleration time series. The effective amplitude spectrum (EAS), defined in the Pacific Earthquake Engineering Research–Next Generation Attenuation (PEER NGA)-East project (Goulet *et al.*, 2018), is calculated for each orthogonal pair of FAS using

$$\text{EAS}(f) = \sqrt{\frac{1}{2}[\text{FAS}_{\text{HC1}}(f)^2 + \text{FAS}_{\text{HC2}}(f)^2]}, \qquad (5)$$

in which FAS_{HC1} and FAS_{HC1} are the FAS of the two orthogonal horizontal components of a three-component time series. The EAS is independent of the orientation of the instrument, and in this way is compatible with the PEER RVT approach for developing orientation-independent PSA predictions (Goulet *et al.*, 2018). We smooth the EAS using the $\log_{10}$-scale Konno and Ohmachi (1998) smoothing window, which has weights and window parameter defined as follows:

$$W(f) = \left(\frac{\sin(b \log(f/f_c))}{b \log(f/f_c)}\right)^4, \qquad (6)$$

$$b = 2\pi/b_w. \qquad (7)$$

The smoothing parameters (W, f_c, b, b_w) are described in Kottke *et al.* (2018). The Konno and Ohmachi smoothing window was selected by PEER NGA-East because it led to minimal bias on the amplitudes of the smoothed EAS when compared to the unsmoothed EAS. The bandwidth of the smoothing window, $b = 188.5$, was selected such that the RVT calibration properties before and after smoothing were minimally affected (Kottke *et al.*, 2018). We use the smoothed EAS with the same smoothing parameters as described in Kottke *et al.* (2018), which has a direct impact on ρ_ϵ. By using the smoothed EAS, we maintain consistency with the PEER database and with other PEER projects, including the NGA-East empirical FAS models (Goulet *et al.*, 2018) and the J. Bayless and N. A. Abrahamson (unpublished manuscript, 2018, see Data and Resources) EAS model.

The simulation residuals were computed relative to the EAS GMM developed by the authors (J. Bayless and N. A. Abrahamson, unpublished manuscript, 2018, see Data and Resources). The simulation residuals are partitioned as given by:

$$\ln(\text{EAS Residual})_{\text{es}}(f)$$
$$= \delta B_e(f) + \delta S2S_s(f) + \delta WS_{es}(f) + C(f), \quad (8)$$

in which $C(f)$ is the mean residual between the suite of simulations and the empirical EAS GMM. The overall bias exists because the median EAS from the simulations is different from the empirical model for a given scenario. We remove the overall bias between the simulations and the empirical model by removing $C(f)$. To avoid overfitting the simulations, which would artificially decrease the computed correlations, we partition the $C(f)$ term into two terms: $C_{\text{fit}}(f)$, the smooth linear fit in log–frequency space to $C(f)$, and $\Delta C(f)$, the remaining bias, termed the method-bias:

$$\ln(\text{EAS Residual})_{\text{es}}(f)$$
$$= \delta B_e(f) + \delta S2S_s(f) + \delta WS_{es}(f) + C_{\text{fit}}(f) + \Delta C(f),$$
$$(9)$$

$$C(f) = C_{\text{fit}}(f) + \Delta C(f). \quad (10)$$

This procedure achieves the goal of fitting the simulation data in a way that is consistent with the procedure for developing an empirical GMM, and gives us residuals from the simulations that are consistent with the empirical residuals (i.e., are approximately normally distributed with zero mean). The bias terms for the six simulation methods evaluated are summarized in Figure 8. The cause of the method-bias is not clear; it could result from the theoretical 1D Green's functions, or it may be introduced by the source representation, for example. The correlation of this bias is included in the total correlation by modifying equation (2) into equation (11).

namely, that there is no variability in the site response because all sites have the same site adjustment. This means we cannot distinguish $\delta S2S$ from the constant:

$$\ln(\text{EAS Residual})_{\text{es}}(f)$$
$$= \delta B_e(f) + \delta WS_{es}(f) + [\delta S2S_s(f) + C(f)]. \quad (13)$$

Stafford (2017) and J. Bayless and N. A. Abrahamson (unpublished manuscript, 2018, see Data and Resources) both found that a significant contribution to the total correlations comes from the between-site terms. As a result, the most appropriate comparison for tuning the methods based on a 1D assumption is the correlation of the between-event and within-site terms, because they can be separated and compared directly. If these methods were tuned to the total correlation, the resulting within-site and between-event components would be overestimated because the between-site correlation component is relevant but cannot be determined for a 1D simulation.

The LLNL simulations, which use a 3D earth structure including surface topography, have the potential to overcome this limitation of 1D modeling; however, because the simulation data provided to us include one realization of the source (e.g., one earthquake scenario and one simulated time history per site), the between-event correlations cannot be estimated or separated from the constant. We also cannot separate the $\delta S2S$ and δWS terms (equation 14).

$$\ln(\text{EAS Residual})_{\text{es}}(f)$$
$$= [\delta S2S_s(f) + \delta WS_{es}(f)] + [\delta B_e(f) + C(f)] \quad (14)$$

In this case, the method-bias term includes one realization of the between-event term. Because the residual components

$$\rho_{\epsilon,\text{total}}(f_1, f_2) = \frac{[\rho_B(f_1, f_2)\tau(f_1)\tau(f_2) + \rho_{S2S}(f_1, f_2)\phi_{S2S}(f_1)\phi_{S2S}(f_2) + \rho_{WS}(f_1, f_2)\phi_{ss}(f_1)\phi_{ss}(f_2) + \rho_{\Delta C}(f_1, f_2)\theta_{\Delta C}\theta_{\Delta C}]}{\sigma_{\text{total}}(f_1)\sigma_{\text{total}}(f_2)},$$
$$(11)$$

in which $\rho_{\Delta C}$ and $\theta_{\Delta C}$ are the auto correlation and standard deviation of the method-bias term, respectively, and σ_{total} is the total standard deviation including the contribution from ΔC (equation 12):

$$\sigma_{\text{total}}^2 = \tau^2 + \phi_{S2S}^2 + \phi_{ss}^2 + \theta_{\Delta C}^2. \quad (12)$$

We carefully select the appropriate components of the correlation model when making comparisons between the empirical ρ_{ϵ} and the ρ_{ϵ} of simulations, so that the conclusions drawn are meaningful. To facilitate this, we provide comparisons between each of the available correlation components and the total correlation. For the BBP simulations, which are based on regionalized 1D earth models without site effects, the between-site component of the correlation is not captured. This is because of an inherent limitation of 1D simulations,

cannot be separated, we compare the total correlation of these simulations with the total correlation from the data. Our conclusions would be strengthened by having more earthquake simulation scenarios to evaluate the correlation components individually.

For both the SCEC and LLNL simulations, the quantity of simulation stations is large enough to robustly estimate the correlation coefficients for a given scenario. For the SCEC simulations, multiple source realizations of the same earthquake are utilized as separate events with respect to calculating residuals. We tested two approaches for calculating ρ_{ϵ} from the simulations. First, we calculated the correlations for individual validation events. Second, we combined the residuals from the nine events into one database before calculating ρ_{ϵ}. We did not observe any systematic differences in the correlations between these approaches, indicating that the
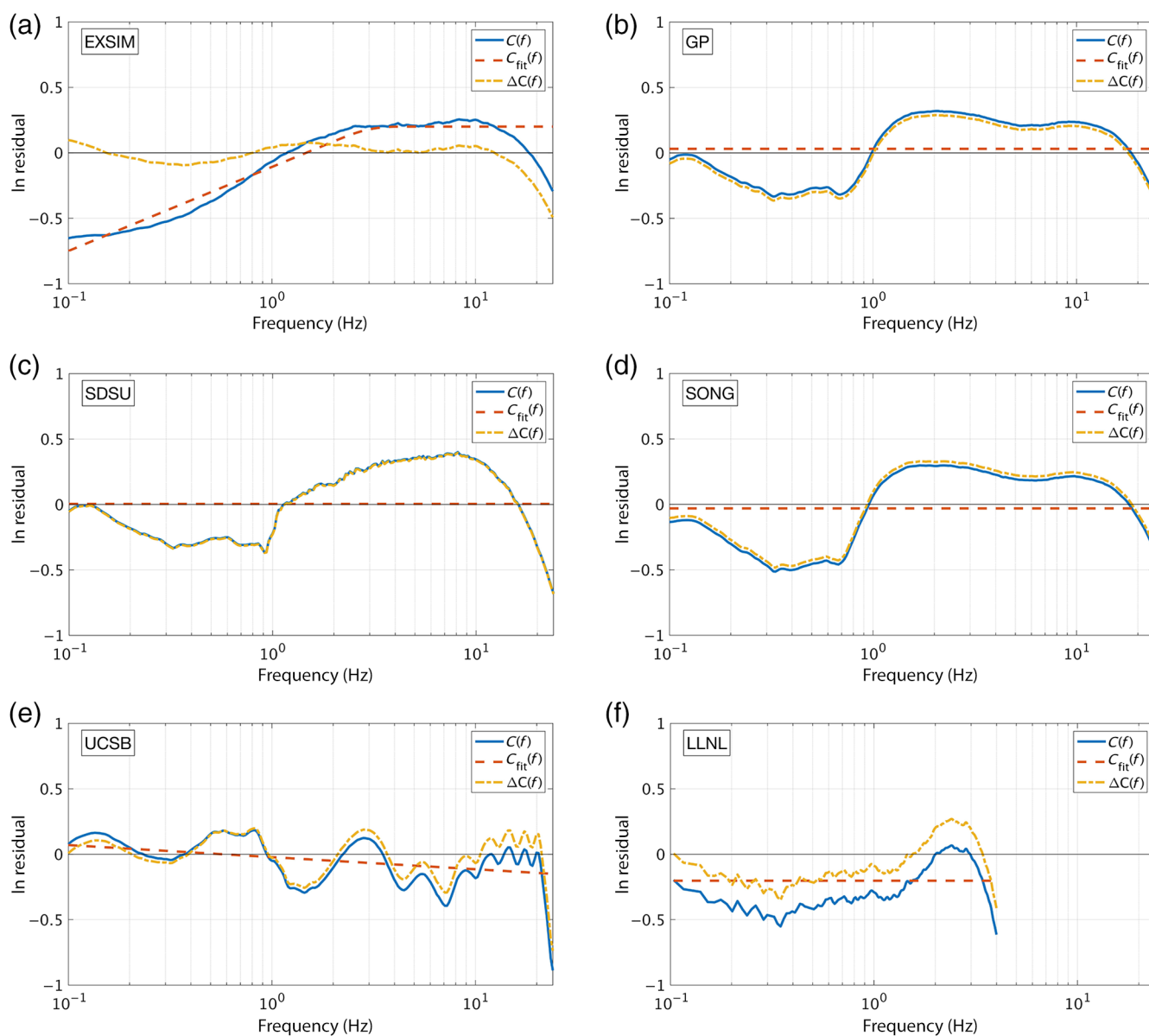
Figure 8. The overall bias between the simulations and the empirical model $C(f)$, the smooth linear fit in log–frequency space $C_{\text{fit}}(f)$, and the remaining model term bias $\Delta C(f)$ for the six simulation methods evaluated: (a) EXSIM (b) GP (c) SDSU (d) SONG (e) UCSB and (f) LLNL. The color version of this figure is available only in the electronic edition.

correlation behavior of the simulations is not event specific. Results shown herein are for the combined database approach. J. Bayless and N. A. Abrahamson (unpublished manuscript, 2018, see Data and Resources) also showed that the interfrequency EAS correlations calculated using recorded data from only the nine SCEC validation events did not vary systematically from the correlations calculated from the full database. This also indicates that the correlations are not event or magnitude specific and that using simulations from a small group of earthquake scenarios should still yield correlations that are broadly consistent with the ρ_{EAS} empirical model.

The J. Bayless and N. A. Abrahamson (unpublished manuscript, 2018, see Data and Resources) total correlation model for EAS is summarized in Figure 9a. The Baker and

Jayaram (2008) model for ρ_{PSA} from shallow crustal earthquakes is shown in Figure 9b. An important difference between the EAS and PSA correlations is the behavior at high frequencies. The PSA contours broaden substantially at high frequencies; this is because of the wide ground-motion frequency range of influence on the short-period PSA, as described in J. Bayless and N. A. Abrahamson (unpublished manuscript, 2018, see Data and Resources). The EAS contours do not exhibit this behavior because the Fourier transform operation at each frequency bin is independent of neighboring bins. Stafford (2017) also developed an interfrequency correlation model for FAS. This model is based on different data and assumptions than the J. Bayless and N. A. Abrahamson (unpublished manuscript, 2018, see Data and
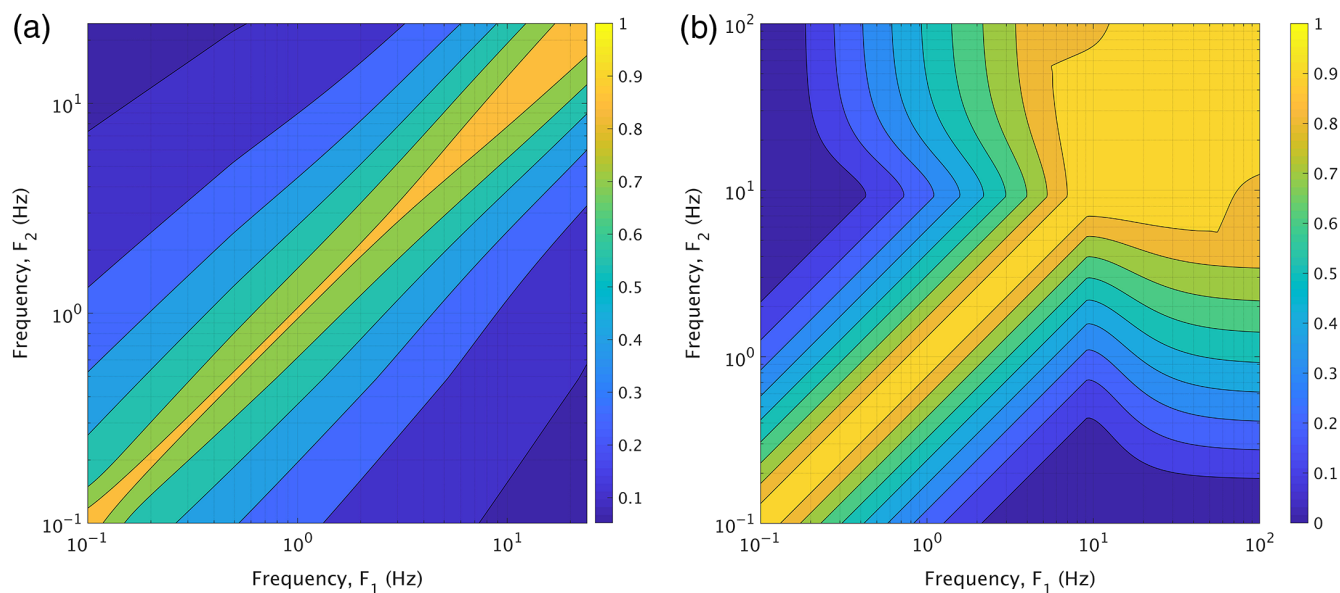
Figure 9. (a) J. Bayless and N. A. Abrahamson (unpublished manuscript, 2018, see Data and Resources) total (effective amplitude spectrum [EAS]) correlation model contours. (b) Baker and Jayaram (2008) PSA correlation model contours. The color version of this figure is available only in the electronic edition.

Resources) model, including using the FAS without smoothing. These differences are discussed in detail in J. Bayless and N. A. Abrahamson (unpublished manuscript, 2018, see Data and Resources). The J. Bayless and N. A. Abrahamson (unpublished manuscript, 2018, see Data and Resources) correlation model is consistent with the empirical EAS datasets developed at PEER and has ρ_ϵ components for the three residual components described previously (δB, $\delta S2S$, and δWS), along with a total correlation model.

Interperiod Correlations

This article evaluates the current status of the correlation contained in the simulation methods described previously. Evaluations are performed primarily in the frequency domain so that shortcomings can be resolved by future improvement to the simulation methods. The specific parts of the simulation methods driving the correlation are yet to be determined, and although the results shown here provide some insights, we believe more work is still needed to identify the causal features. Therefore, we focus on presenting the results without concluding which features of the simulations control the correlation.

Figures 10–14 summarize the ρ_{EAS} and ρ_{PSA} of the five BBP simulation methods evaluated, using the nine validation event simulations, and with residuals calculated using J. Bayless and N. A. Abrahamson (unpublished manuscript, 2018, see Data and Resources) for the EAS, and the Next Generation Attenuation-West2 Project GMMs for PSA. These figures provide a visual means of subjectively comparing the correlations calculated from the simulation methods with the empirical correlations. Each figure shows cross sections of the ρ_ϵ contours at conditioning frequencies 0.2, 0.5, 2, 5, and 15 Hz.

Panels (a–c) of each figure compare the cross sections of the between-event, within-site, and total ρ_{EAS} with empirical correlations, respectively. Panel (d) compares the ρ_{PSA} with the Baker and Jayaram model. We focus our comparisons to correlations greater than 0.4, because we expect that the correlation values greater than about 0.5 impact the structural response. As mentioned previously, the BBP simulations are based on regionalized 1D earth models without site effects, so the between-site component of the correlation is not captured. Figure 15 presents the same summary of the correlations calculated from the LLNL simulations, in which the empirical ρ_ϵ cross sections represent the total correlation model.

EXSIM method results are shown in Figure 10. As expected, because EXSIM is based on the PS stochastic method, the within-site and total interperiod correlations for this method are lower than the empirical correlations and drop rapidly, moving away from the conditioning frequency. The between-event correlation conditioned at 15 Hz (Fig. 10a) is broad relative to other frequencies; we observe similar relatively high between-event correlation at the higher frequencies for several of the simulation methods. The within-event ρ_{PSA} observed is generally consistent with the conclusions of Burks and Baker (2014).

Figure 11 displays the GP method results. At frequencies above 1 Hz, this method is similar to EXSIM, and the within-site correlations are therefore similarly low. At frequencies below 1 Hz, the correlations generally show significant promise, but the total ρ_{EAS} values still drop off too quickly, moving away from the conditioning frequency for most frequencies. At frequencies less than about 0.25 Hz, the total correlations are similar to the empirical correlations. By definition, the PSA correlations reflect the EAS correlations. This is evident for GP as the short-period (<1 s)
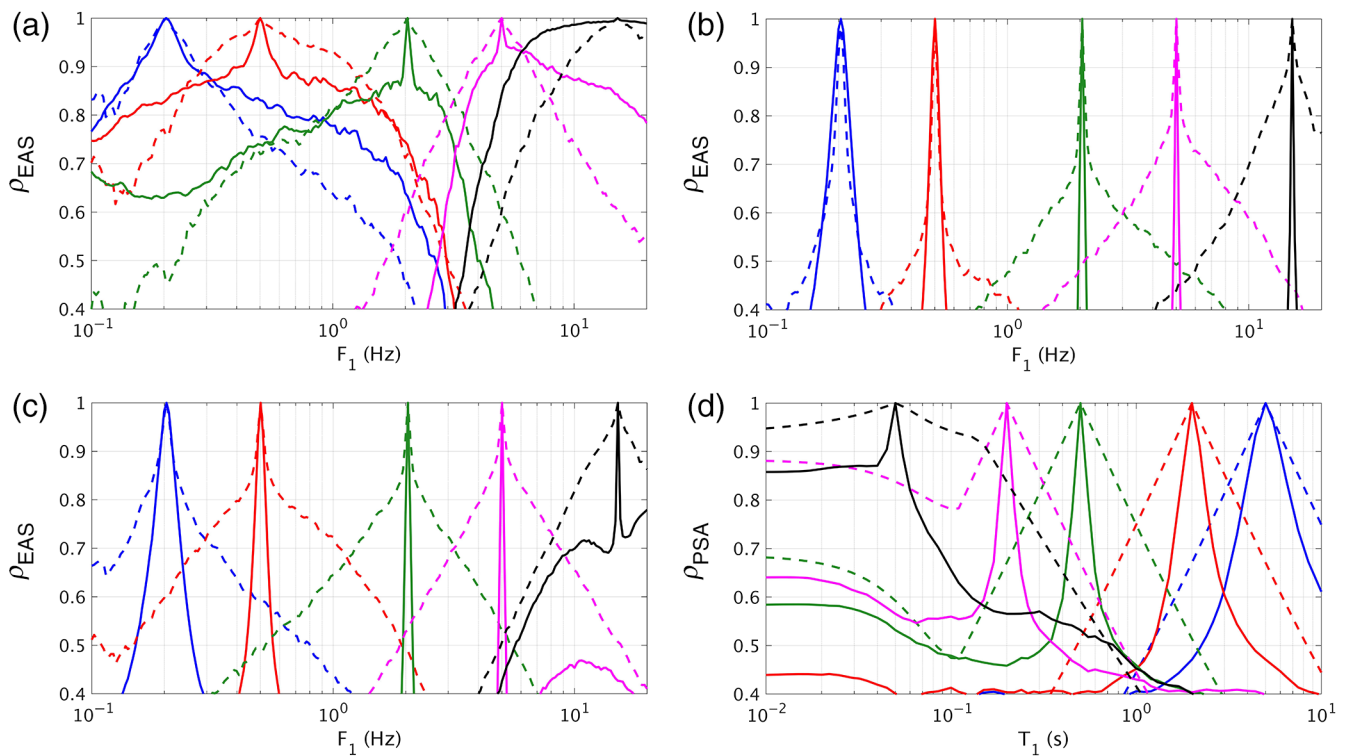
Figure 10.   Summary of the correlations calculated from the Atkinson and Assatourians (2015) Southern California Earthquake Center (SCEC) Broadband Platform (BBP) validation simulations, compared with empirical correlations. (a) Between-event ρ_{EAS} cross sections versus frequency at conditioning frequencies 0.2, 0.5, 2, 5, and 15 Hz (solid lines), compared with the empirical correlations from J. Bayless and N. A. Abrahamson (unpublished manuscript, 2018, see Data and Resources) (dashed lines). (b) Comparison of the within-site ρ_{EAS}. (c) Comparison of the total ρ_{EAS}. (d) Within-event ρ_{PSA} cross sections versus period (solid lines), compared with the Baker and Jayaram (2008) model (dashed lines). The color version of this figure is available only in the electronic edition.

RotD50 correlations are low, and the long period (>1 s) ones are closer to the empirical model. The within-event ρ_{PSA} for the GP method is also generally consistent with those calculated by Burks and Baker (2014).

SDSU method results are shown in Figure 12. At frequencies below 1 Hz, this method is identical to GP, and therefore the correlations are the same as GP. At higher frequencies, this method shows an abrupt drop of the within-site correlation away from the conditioning frequency, followed by moderately high correlation (between 0.7 and 0.95) over the entire frequency range greater than 1 Hz. The cause of this feature is currently unknown and should be studied further.

Figure 13 displays the SONG method results. The SONG method uses the GP wave propagation and simulation code; the only differences are in the earthquake source. Including this method in our analysis is a convenient way to isolate the effects of the correlation of earthquake source parameters on the GP simulation method interfrequency correlations. The SONG earthquake source method is characterized by kinematic source parameters (including slip, rupture velocity, peak slip velocity) with 1-point statistics (median and standard deviation) and 2-point statistics (autocorrelation in space and correlation between parameters) constrained by dynamic rupture modeling. Because the SONG low-frequency correlations are significantly broader than the GP

correlations, this indicates that correlation of these parameters in the source may have an important effect on the low-frequency interperiod correlations. Similar to GP, the SONG total correlations are closest to the empirical model at low frequencies, and actually exceed the empirical correlations at frequencies very near the conditioning frequency. The total correlations are low at the high frequencies. This model is the only one evaluated that potentially overestimates the total ρ_{EAS} over a wide range of frequencies (approximately 0.1–0.7 Hz).

Figure 14 displays the UCSB method results. This model, similar to several others, has lower within-site correlation than the empirical models at frequencies above 1 Hz. Similarly, the low-frequency total correlations are closer, but still slightly low, compared to the data, except for very low frequencies in which they are similar to the empirical correlations. The between-event ρ_{EAS} at high frequencies is much broader than the empirical models, and this effect propagates through to the total ρ_{EAS}. We also observe an undulating pattern in the ρ_{EAS}, especially for low-correlation values at frequencies far from the conditioning frequency. This pattern was not observed with the other methods, but the higher correlation values will have the most effect on structural response; therefore we believe that the undulating feature at low-correlation values is not a concern with respect to validation.
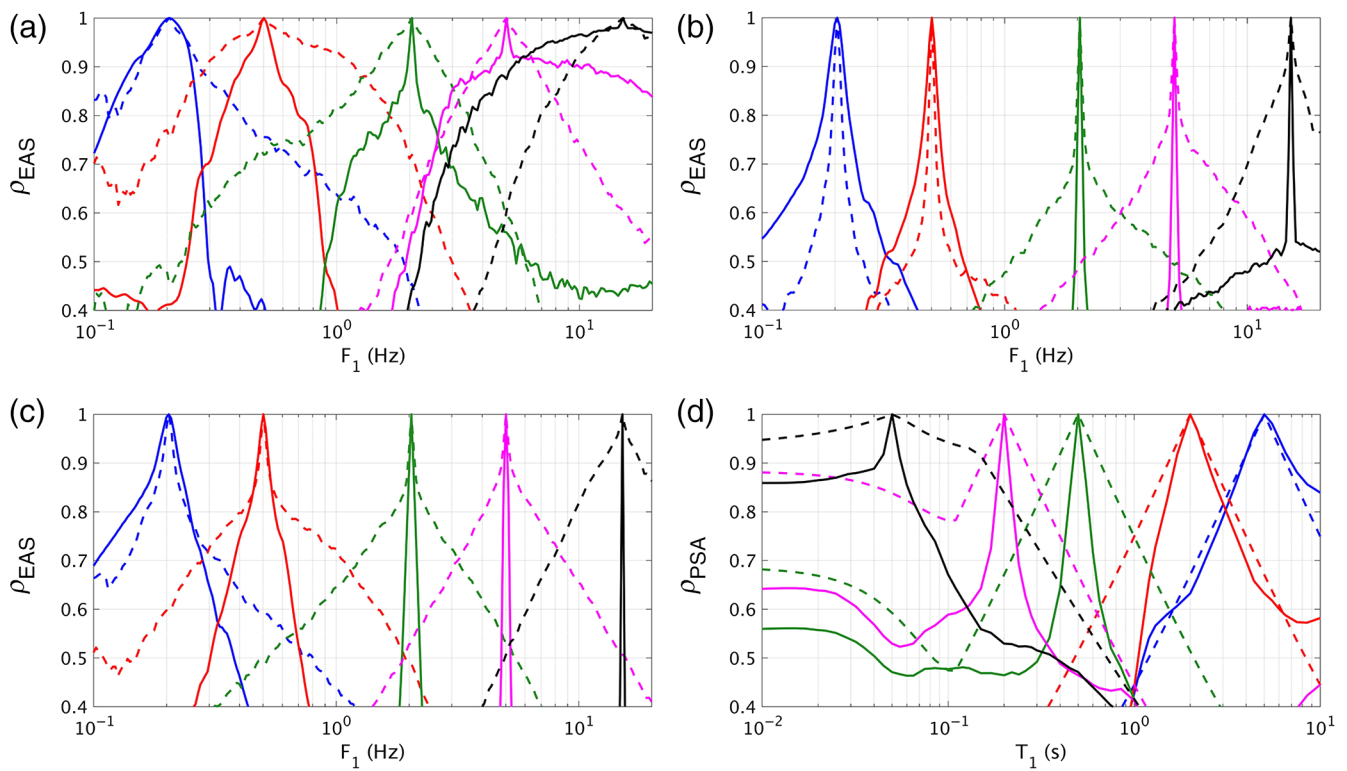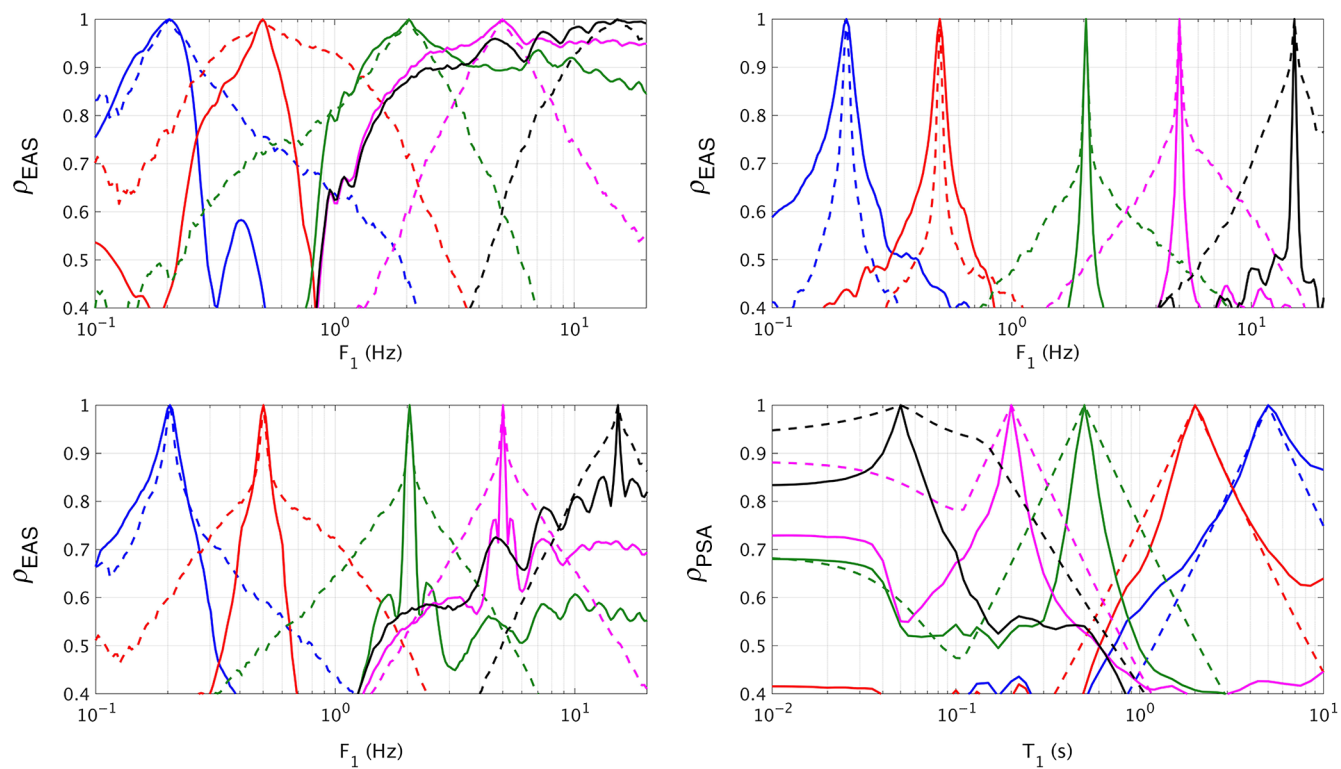
Figure 11. Summary of the correlations calculated from the Graves and Pitarka (2015) SCEC BBP validation simulations. See Figure 10 caption for a complete description. The color version of this figure is available only in the electronic edition.
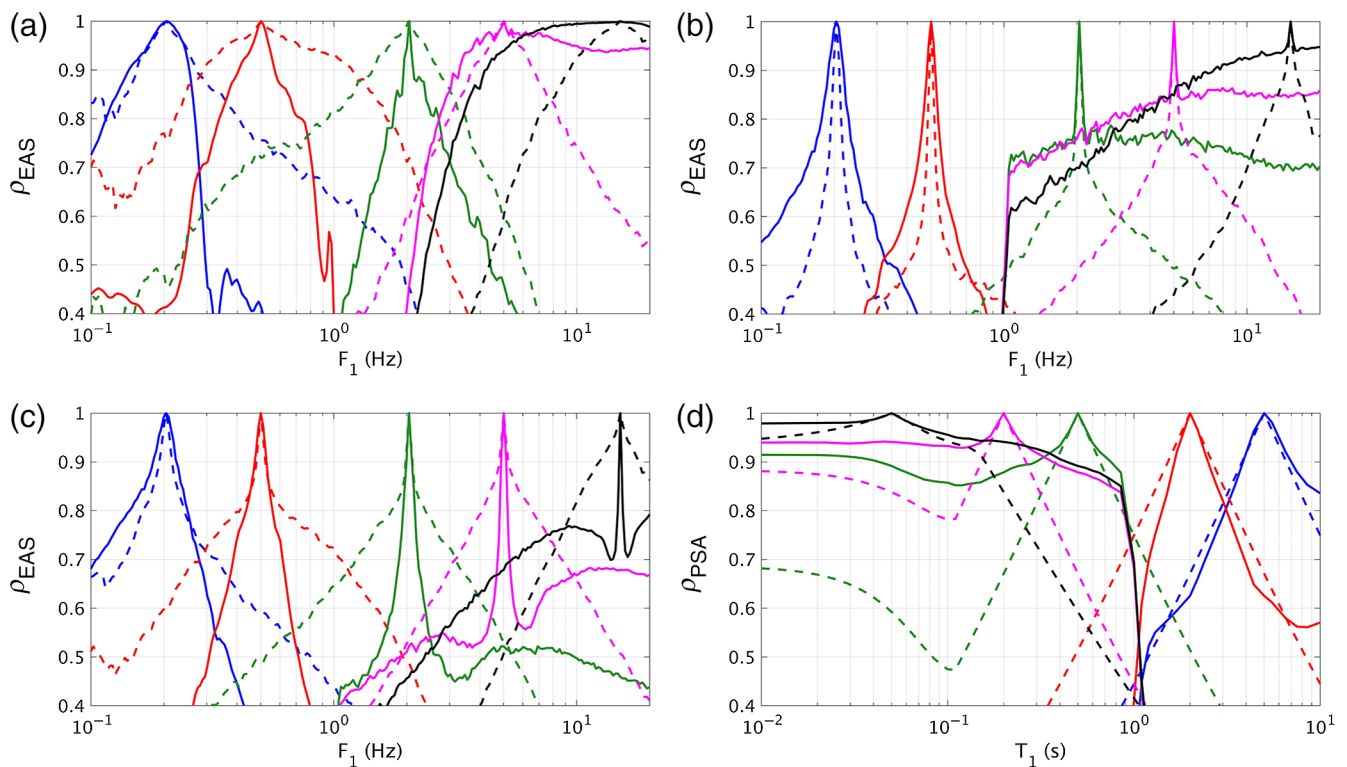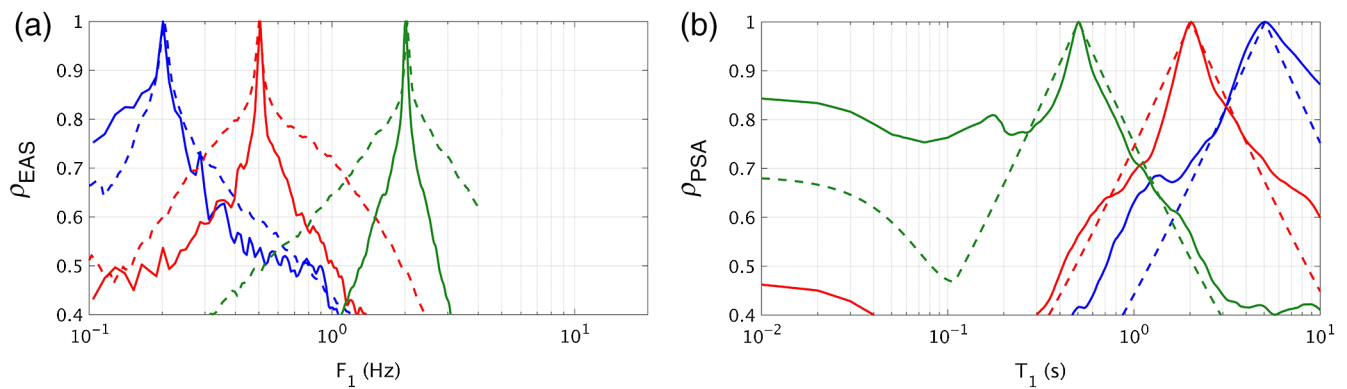

Figure 12. Summary of the correlations calculated from the Olsen and Takedatsu (2015) SCEC BBP validation simulations. See Figure 10 caption for a complete description. The color version of this figure is available only in the electronic edition.
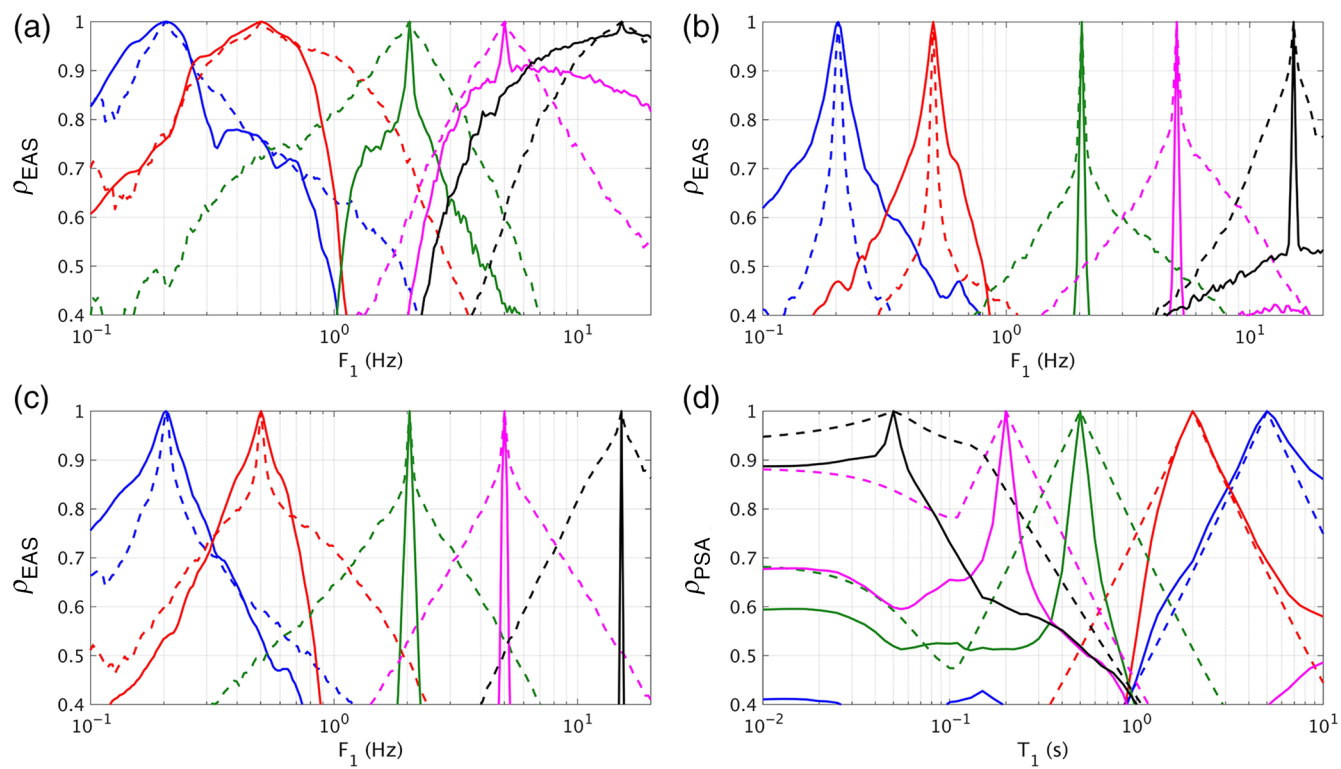
Figure 13. Summary of the correlations calculated from the Song (2016) SCEC BBP validation simulations. See Figure 10 caption for a complete description. The color version of this figure is available only in the electronic edition.

Figure 14. Summary of the correlations calculated from the Crempien and Archuleta (2015) SCEC BBP validation simulations. See Figure 10 caption for a complete description. The color version of this figure is available only in the electronic edition.

Figure 15. Summary of the correlations calculated from the Rodgers *et al.* (2018) Hayward fault scenario simulations at conditioning frequencies 0.2, 0.5, and 2 Hz. See Figure 10 caption for a complete description. The color version of this figure is available only in the electronic edition.

Figure 15 displays the LLNL method results over the frequency range 0.1–4 Hz. As described previously, these simulations are for one realization of the source, so the between-event and between-site correlations cannot be separated. Therefore, the correlations we calculate include one realization of the between-event correlation in addition to the remaining correlation, and so we compare with the total correlation model. These results show a similar trend to the other methods analyzed; the broadest correlations at lowest frequencies, with too steeply dropping correlations at higher frequencies. At the lowest frequencies, the total correlations are similar to those from the data, but further refinements should be made to frequencies greater than about 0.25 Hz. Our conclusions regarding the LLNL simulations would be strengthened by having more earthquake simulation scenarios to evaluate the correlation components individually.

Conclusions

The interperiod correlation of epsilon (ρ_ϵ) is an important component of ground motions for capturing the variability of structural response that is needed in seismic fragility and seismic risk studies. Without the adequate interperiod correlation of ground motions, variability in the structural response may be underestimated. This leads to structural fragilities that are too steep (underestimated dispersion parameter β) and propagate to nonconservative estimates of seismic risk. The conclusions herein apply directly to structural fragility or risk assessments derived from ground-motion simulations, commonly referred to as ruptures to rafters simulations. These results were similar for the three structures analyzed: a six-story steel SMRF, a 12-story reinforced concrete building, and a typical California Department of Transportation highway overcrossing.

None of the six finite-fault simulation methods tested adequately capture the interperiod correlations over the entire frequency range evaluated, although several of the methods show promise, especially at low frequencies. Using the correlation of the EAS provides the developers of the simulation methods better feedback in terms of how they can

modify their methods, which is unclear when using PSA comparisons. For the stochastic part of the simulation, adding the empirical correlation is relatively straightforward, such as was done for the stochastic simulations used here. For the deterministic part of the simulation, capturing the correlation is more difficult as it requires modifying the rupture generator or the wave propagation parts of the simulation that have already been validated for the median ground motion. Based on the relative differences in the correlations of the SONG source method, it appears that changes to the rupture generator may be the most promising approach to modifying the long-period interperiod correlations.

Data and Resources

Analyses and graphics production were performed using the numeric computing environment MATLAB (www.mathworks.com, last accessed October 2018). Fourier spectra were computed using Dave Boore's collection of time series processing programs (www.daveboore.com, last accessed October 2018). Structural analyses were performed using the open-source software OpenSees (opensees.berkeley.edu, last accessed October 2018). All simulations were obtained by personal communication with the corresponding authors or with Southern California Earthquake Center (SCEC). Unpublished manuscript by J., Bayless and N. A. Abrahamson (2018), "An empirical model for Fourier amplitude spectra using the NGA-West2 database," in preparation.

Acknowledgments

References

Abrahamson, N. A., W. J. Silva, and R. Kamai (2014). Summary of the ASK14 ground motion relation for active crustal regions, *Earthq. Spectra* **30,** 1025–1055, doi: 10.1193/070913EQS198M.

Akkar, S., M. A. Sandıkkaya, and B. Ö. Ay (2014). Compatible ground-motion prediction equations for damping scaling factors and vertical-to-horizontal spectral amplitude ratios for the broader Europe region, *Bull. Earthq. Eng.* **12,** 517–547, doi: 10.1007/s10518-013-9537-1.

Al Atik, L. (2011). Correlation of spectral acceleration values for subduction and crustal models, *COSMOS Technical Session*, Emeryville, California, 4 November.

Al Atik, L., N. A. Abrahamson, F. Cotton, F. Scherbaum, J. J. Bommer, and N. Kuehn (2010). The variability of ground-motion prediction models and its components, *Seismol. Res. Lett.* **81,** no. 5, 794–801.

American Society of Civil Engineers (ASCE) (2016). Minimum design loads for buildings and other structures, *ASCE/SEI Standard 7–16*, 206 p.

Anderson, J. G. (2015). The composite source model for broadband simulations of strong ground motions, *Seismol. Res. Lett.* **86,** 68–74, doi: 10.1785/0220140098.

Atkinson, G. M., and K. Assatourians (2015). Implementation and validation of EXSIM (A stochastic finite-fault ground-motion simulation algorithm) on the SCEC broadband platform, *Seismol. Res. Lett.* **86,** 48–60.

Azarbakht, A., M. Mousavi, M. Nourizadeh, and M. Shahri (2014). Dependence of correlations between spectral accelerations at multiple periods on magnitude and distance, *Earthq. Eng. Struct. Dynam.* **43,** 1193–1204.

Baker, J. W. (2013). Trade-offs in ground motion selection techniques for collapse assessment of structures, *Vienna Congress on Recent Advances in Earthquake Engineering and Structural Dynamics*, Vienna, Austria, 30 August.

Baker, J. W., and B. A. Bradley (2017). Intensity measure correlations observed in the NGA-West2 database, and dependence of correlations on rupture and site parameters, *Earthq. Spectra* **33,** no. 1, 145–156.

Baker, J. W., and C. A. Cornell (2006). Correlation of response spectral values for multi-component ground motions, *Bull. Seismol. Soc. Am.* **96,** no. 1, 215–227.

Baker, J. W., and N. Jayaram (2008). Correlation of spectral acceleration values from NGA ground motion models, *Earthq. Spectra* **24,** 299–317, doi: 10.1193/1.2857544.

Boore, D. M. (1983). Stochastic simulation of high-frequency ground motions based on seismological models of the radiated spectra, *Bull. Seismol. Soc. Am.* **73,** 1865–1894.

Boore, D. M. (2003). Simulation of ground motion using the stochastic method, *Pure Appl. Geophys.* **160,** 635–675.

Boore, D. M., and E. M. Thompson (2012). Empirical improvements for estimating earthquake response spectra with random-vibration theory, *Bull. Seismol. Soc. Am.* **102,** no. 2, 761–772.

Bradford, S. C. (2007). Time-frequency analysis of systems with changing dynamic properties, *Ph.D. Dissertation*, California Institute of Technology, Pasadena, California.

Brune, J. N. (1970). Tectonic stress and spectra of seismic shear waves from earthquakes, *J. Geophys. Res.* **75,** 4997–5009.

Burks, L. S., and J. W. Baker (2014). Validation of ground motion simulations through simple proxies for the response of engineered systems, *Bull. Seismol. Soc. Am.* **104,** no. 4 1930–1946.

Cimellaro, G. P. (2013). Correlation in spectral accelerations for earthquakes in Europe, *Earthq. Eng. Struct. Dynam.* **42,** 623–633, doi: 10.1002/eqe.2248.

Crempien, J. G. F., and R. J. Archuleta (2015). UCSB method for simulation of broadband ground motion from kinematic earthquake sources, *Seismol. Res. Lett.* **86,** 61–67, doi: 10.1785/0220140103.

Dreger, D. S., and T. H. Jordan (2014). Introduction to the focus section on validation of the SCEC broadband platform V14.3 simulation methods, *Seismol. Res. Lett.* **86,** no. 1, 15–16, doi: 10.1785/0220140233.

Dreger, D. S., G. C. Beroza, S. M. Day, C. A. Goulet, T. H. Jordan, P. A. Spudich, and J. P. Stewart (2015). Validation of the SCEC broadband platform V14.3 simulation methods using pseudospectral acceleration data, *Seismol. Res. Lett.* **86,** no. 1, doi: 10.1785/0220140118.

Fisher, R. A. (1958). *Statistical Methods for Research Workers*, 13th Ed., Hafner, Edinburgh, London, United Kingdom.

Goda, K, and G. M. Atkinson (2009). Probabilistic characterization of spatially correlated response spectra for earthquakes in Japan, *Bull. Seismol. Soc. Am.* **99,** 3003–3020, doi: 10.1785/0120090007.

Goulet, C. A., N. A. Abrahamson, P. G. Somerville, and K. E. Wooddell (2015). The SCEC broadband platform validation exercise: Methodology for code validation in the context of seismic-hazard analyses, *Seismol. Res. Lett.* **86,** no. 1, doi: 10.1785/0220140104.

Goulet, C. A., A. Kottke, D. M. Boore, Y. Bozorgnia, J. Hollenback, T. Kishida, A. Der Kiureghian, O. J. Ktenidou, N. M. Kuehn, E. M. Rathje, *et al.* (2018). Effective amplitude spectrum (EAS) as a metric for ground motion modeling using Fourier amplitudes, *2018 Seismology of the Americas Meeting*, Miami, Florida, 14–17 May 2018.

Graves, R., and A. Pitarka (2015). Refinements to the Graves and Pitarka (2010) broadband ground-motion simulation method, *Seismol. Res. Lett.* **86,** 75–80, doi: 10.1785/0220140101.

Hanks, T. C., and R. K. McGuire (1981). The character of high-frequency strong ground motion, *Bull. Seismol. Soc. Am.* **71,** 2071–2095.

Heo, Y. A. (2009). Framework for damage-based probabilistic seismic performance evaluation of reinforced concrete frames, *Ph.D. Dissertation*, University of California, Davis.

Jayaram, N., J. W. Baker, H. Okano, H. Ishida, M. W. McCann, and Y. Mihara (2011). Correlation of response spectral values in Japanese ground motions, *Earthq. Struct.* **2,** no. 4, 357–376.

Kalkan, E., and S. K. Kunnath (2006). Effects of fling step and forward directivity on seismic response of buildings, *Earthq. Spectra* **22,** no. 2, 367–390.

Konno, K., and T. Ohmachi (1998). Ground-motion characteristics estimated from spectral ratio between horizontal and vertical components of microtremor, *Bull. Seismol. Soc. Am.* **88,** 228–241.

Kottke, A., E. Rathje, D. M. Boore, E. Thompson, J. Hollenback, N. Kuehn, C. A. Goulet, N. A. Abrahamson, Y. Bozorgnia, and A. Der Kiureghian (2018). Selection of random vibration procedures for the NGA East project, *PEER Report 2018-05*.

Kunnath, S. K, E. Erduran, Y. H. Chai, and M. Yashinsky (2008). Effect of near-fault vertical ground motions on seismic response of highway overcrossings, *J. Bridge Eng.* **13,** no. 3, 282–290.

Kunnath, S. K., Q. Nghiem, and S. El-Tawil (2004). Modeling and response prediction in performance-based seismic evaluation: Case studies of instrumental steel moment-frame buildings, *Earthq. Spectra* **20,** no. 3, 883–915.

Lin, L., N. Naumoski, S. Foo, and M. Saatcioglu (2008). Elongation of the fundamental periods of reinforced concrete frame buildings during nonlinear seismic response, presented at the *14th World Conf. Earthquake Engineering*, Beijing, China, 12–17 October.

Maechling, P. J., F. Silva, S. Callaghan, and T. H. Jordan (2015). SCEC broadband platform: System architecture and software implementation, *Seismol. Res. Lett.* **86,** no. 1, doi: 10.1785/0220140125.

McKenna, F., M. H. Scott, and G. L. Fenves (2010). Nonlinear finite element analysis software architecture using object composition, *J. Comput. Civil Eng.* **24,** no. 1, 95–107.

Moehle, J. P., and G. G. Deierlein (2004). A framework methodology for performance-based earthquake engineering, Paper presented at the *13th World Conference on Earthquake Engineering*, Vancouver, Canada.

Olsen, K. B., and R. Takedatsu (2015) The SDSU broadband ground-motion generation module BBtoolbox Version 1.5, *Seismol. Res. Lett.* **86,** 81–88, doi: 10.1785/0220140102.

Rodgers, A. J., A. Pitarka, N. A. Petersson, B. Sjogree, and D. B. McCallen (2018). Broadband (0–4 Hz) ground motions for a magnitude 7.0 Hayward fault earthquake with three-dimensional structure and topography, *Geophys. Res. Lett.* **45,** 739–747, doi: 10.1002/2017GL076505.

Seydel, R. U. (2012). *Tools for Computational Finance*, Universitext, Springer-Verlag, London, United Kingdom.

Song, S. G. (2016). Developing a generalized pseudo-dynamic source model of M_w 6.5–7.0 to simulate strong ground motions, *Geophys. J. Int.* **204,** 1254–1265, doi: 10.1093/gji/ggv521.

Stafford, P. J. (2017). Inter-frequency correlations among Fourier spectral ordinates and implications for stochastic ground-motion simulation, *Bull. Seismol. Soc. Am.* **107,** no. 6, 2774–2791.

Tothong, P., and C. A. Cornell (2006). An empirical ground-motion attenuation relation for inelastic spectral displacement, *Bull. Seismol. Soc. Am.* **96,** no. 6, 2146–2164.

Villani, M. A., and N. Abrahamson (2015). Repeatable site and path effects on the ground-motion sigma based on empirical data from Southern California and simulated waveforms from the Cyber-Shake platform, *Bull. Seismol. Soc. Am.* **105,** doi: 10.1785/0120140359.

Department of Civil and Environmental Engineering
One Shields Avenue
University of California, Davis
Davis, California 95616
jrbayless@ucdavis.edu
(J.B.)

Department of Civil Engineering
University of California, Davis
Davis, California 95616
(N.A.A.)